

# The Variable Diffuse Continuum Emission of Broad Line Clouds

Kirk T. Korista<sup>1</sup>

*Department of Physics, Western Michigan University*

*Kalamazoo, MI 49008-5252*

korista@wmich.edu

and

Michael R. Goad<sup>2</sup>

*Department of Physics and Astronomy, University of Leicester*

*University Road, Leicester, LE1 7RH, England, UK*

mrg@star.le.ac.uk

## ABSTRACT

We investigate the wavelength-dependent intensity and reverberation properties of the UV-optical diffuse continuum emission expected from broad emission line gas. The “locally optimally-emitting clouds” picture is adopted, with the cloud distribution functions in gas density and distance from the ionizing source determined by a fit to the mean UV emission line spectrum from the 1993 *HST* campaign of NGC 5548 in our previous paper. The model Balmer continuum’s strength and variability characteristics are in agreement with those derived from the observations of NGC 5548. A key prediction is a wavelength-dependent lag across the UV-optical spectrum which can broadly mimic the signature from X-ray reprocessing in an accretion disk, calling into question the discovery claims of the latter in NGC 7469. The influence of the diffuse continuum on the optical continuum may result in a small yet significant underestimation of the characteristic sizes of the regions emitting the optical emission lines. Its contribution can also alter the inferred spectral energy distribution of the UV-optical continuum, even well outside the spectral region near the well-known Balmer jump. The reverberation of the diffuse continuum emitted by the BLR may account for perhaps one-third of the observed effect that the  $\lambda 1350 - \lambda 5100$  continuum becomes bluer as it becomes brighter (even after accounting for non-variable optical starlight). And as in other models of the broad emission line gas, a significant yet unobserved Lyman jump is predicted. We highlight the importance of careful studies of the UV-optical continuum, especially the Balmer continuum.

*Subject headings:* galaxies: active—galaxies: individual (NGC 5548) galaxies:  
nuclei—galaxies: Seyfert—continuum: formation

NGC 5548

## 1. INTRODUCTION

From the early work of Davidson & Netzer (1979) to the more advanced models of Rees, Netzer, & Ferland (1989), Goad, Gondhalekar, & O’Brien (1993), Kaspi & Netzer (1999) and many others, much attention has been given to the theoretical modeling of the prominent broad emission lines of active galactic nuclei (AGN; including quasars) and their variability in order to understand the lines’ origin and the story of the AGN phenomenon. However, with few exceptions (e.g., Davidson 1976; Wamsteker et al. 1990; Maoz et al. 1993) very little has been said about the diffuse continuum emission from the same emitters of the broad lines. Korista et al. (1995; hereafter K95) presented six high signal-to-noise “continuum window” light curves of NGC 5548 between 1145 Å and 2195 Å (rest frame; their Figure 6), and they noted systematic decreases in the variability amplitude and sharpness of the variations. While they could not measure it directly, K95 suspected these characteristics to be the signature of a wavelength-dependent continuum lag, whose origin was either with the continuum source and/or with contaminating diffuse continuum emission from the broad line region (BLR). If the diffuse continuum emitted by broad line clouds is significant, it will have the following impacts on models for the broad emission line region and the UV-optical continuum emitter: (1) the lag between the emission line variations and those of the local “continuum” may underestimate the characteristic sizes of the line emitting regions, (2) the shape of the underlying nuclear continuum may be misinferred and thus misinterpreted, (3) interband continuum lags may be misinterpreted, (4) the reverberation of the diffuse continuum emitted by the BLR may account for perhaps one-third of the observed effect that the  $\lambda 1350 - \lambda 5100$  continuum becomes bluer as it becomes brighter (even after accounting for non-variable optical starlight), and (5) as in other models of the broad emission line gas, a significant yet unobserved Lyman jump is predicted. Here we investigate the importance of the diffuse continuum to the mean and variable light spectra of AGN using the well-studied AGN NGC 5548 as a case in point.

## 2. DIFFUSE CONTINUUM EMISSION FROM THE BROAD LINE REGION

### 2.1. The Photoionization Grid

We adopted the grid of photoionization computations presented in Korista & Goad (2000; hereafter, Paper I) to model the UV broad line emission from NGC 5548. The reader is directed there for details; here we mention some of the salient features of the grid.

Using Ferland’s spectral synthesis code, CLOUDY (v90.04) (Ferland 1997; Ferland et al. 1998) we generated a grid of photoionization models of BEL emitting entities, here assumed to be simple slabs, each of which we assumed has constant gas density and a clear view to the source of ionizing photons. The grid dimensions spanned 7 orders of magnitude in total hydrogen gas number density,  $7 \leq \log n_H(\text{cm}^{-3}) \leq 14$ , and hydrogen-ionizing photon flux,  $17 \leq \log \Phi_H(\text{cm}^{-2} \text{s}^{-1}) \leq 24$ , and stepped in 0.125 decade intervals in each dimension (3,249 separate CLOUDY models). We will refer to the plane defined by these two parameters as the density – flux plane. For the present simulations we assumed all clouds have a single total hydrogen column density,  $N_H = 10^{23} \text{ cm}^{-2}$ . For very low values of the ionization parameter,  $U_H \equiv \Phi_H/n_Hc$ , the cloud computations stopped at an electron temperature of 4000 K rather than at the total hydrogen column density  $10^{23} \text{ cm}^{-2}$ . This artifact had little impact upon the results presented here (or in Paper I), since these clouds contributed little to the light of the model BLR. Descriptions of the slightly sub-solar abundances, the incident continuum spectral energy distribution (SED), and the cloud distribution functions in gas density and radius to model the mean UV spectrum of NGC 5548 are given in Paper I.

For the choice of cosmological parameters from Paper I ( $H_o = 75 \text{ km s}^{-1} \text{ Mpc}^{-1}$ ;  $q_o = 0.5$ ;  $z = 0.0172$ ),  $\log \lambda L_{\lambda 1350} \approx 43.54 \text{ ergs s}^{-1}$  from the mean, dereddened value of  $\lambda F_{\lambda}(1350)$  of the 1993 *HST* campaign. The central continuum SED adopted in Paper I (see also Walter et al. 1994) then finds the mean hydrogen-ionizing luminosity to be  $\log L_{ion} \approx 44.26 \text{ ergs s}^{-1}$ . At this luminosity a  $\log \Phi_H = 20 \text{ cm}^{-2} \text{ s}^{-1}$  corresponds to a distance from the continuum source of  $R \approx 12.6 (75/H_o)$  light-days.

### 2.2. The Diffuse Continuous Emission from Broad-Line Clouds

The diffuse continuum emission includes a component of reflected incident continuum (see Korista & Ferland 1998) in addition to true (i.e., thermal) diffuse, non-line emission from the cloud. The ratios of twelve diffuse continuum band fluxes to the incident continuum flux measured at  $1215 \text{ \AA}$ ,  $\lambda F_{\lambda}(d)/\lambda F_{\lambda 1215}(i)$ , spanning the UV-optical spectrum, are plotted in

contour in the density – flux plane in Figures 1a,b. Lines of constant ionization parameter run at  $45^\circ$  angles from the lower left to the upper right of each panel. In all cases the solid triangle marks the peak ratio. As noted by Rees, Netzer, & Ferland (1989), the high density clouds are efficient emitters of continua.

Across most of the optical-UV spectral region, the diffuse continuum is dominated by hydrogen free-bound emission. The diffuse to incident continuum ratio contours generally run gently downhill diagonally toward the lower left corner, steeply downhill at the highest densities toward low values of  $\log \Phi_H$ , and steeply downhill toward the upper left corner of each panel. This behavior is explained as follows. The ionization parameter increases toward the upper left of each panel, and the gas becomes highly ionized so that the diffuse emission becomes a combination of weak free-free and electron scattering ( $\tau_{es(max)} \lesssim 0.07$  for the cloud column density considered here). Toward the lower left corner, the density diminishes along constant ionization parameter, and emission lines at diminishing optical depth cool the gas more efficiently. Toward the lower right corner, the ionization parameter becomes very small and the electron temperature drops significantly, squelching the exponential nature of the free-bound emission. Toward the upper right the lines become thermalized at large optical depth, and continuum processes (especially free-bound) cool the gas more efficiently. While the diffuse continuum emissivity increases toward high gas densities, that which is emitted at ever shorter wavelengths from a bound-free continuum edge becomes ever more sensitive to the electron temperature due to the Boltzmann factor. The temperature is sensitive to the ionization parameter, and so the emissivity becomes ever more dependent upon the ionizing photon flux as well. Compare in Figure 1 the contour locations and orientations of the  $\lambda 1793$  band to those of the  $\lambda 3644$  Balmer jump. Optical depth effects play a similar though much more minor role in governing the diffuse continuum emission efficiencies in the density – flux plane (Figure 1). For example, the optical depth within the Balmer continuum is always larger nearer to the bandhead at any value of the incident photon flux, and the optical depth increases with increasing incident photon flux due to increased excited state populations of hydrogen and larger emission depths. This has the effect of skewing the emission near the bandhead to larger radii (smaller incident photon fluxes), as compared to those wavelengths lying ever shortward of the bandhead.

The band at  $\lambda 1218$  lies near the peak of the Rayleigh scattering albedo feature whose strength and wavelength width are in proportion to the neutral hydrogen column density (see Korista & Ferland 1998). This feature generally dominates the diffuse continuum at this wavelength. This band’s contours of intensity relative to the incident continuum are essentially flat with a value of  $\approx 1$  (lower-right half of the density – flux plane), since the effective albedo due mainly to Rayleigh scattering is roughly 1 for neutral hydrogen column densities exceeding a few  $\times 10^{20} \text{ cm}^{-2}$ . Also the contrast of the Rayleigh scattering feature

above the “background” (primarily Thomson scattering) albedo changes in near inverse proportion to the Thomson scattering albedo, that is in turn proportional to  $U_H$  for a fixed total column density cloud. At sufficiently large ionization parameters, the hydrogen ionization front emerges out the back ends of the clouds and the Rayleigh scattering feature disappears rapidly (upper-left half of the density – flux plane).

In summary, the diffuse continuum  $\lambda F_\lambda(d)$  for wavelengths longward of  $\text{Ly}\alpha$  is near a minimum at the  $\lambda 1458$  band, while it reaches its maximum at the Balmer jump for gas densities exceeding  $10^{10} \text{ cm}^{-3}$ , and at the Rayleigh scattering feature for lower gas densities.

### 2.3. The Observed UV-Optical Spectrum of NGC 5548

We placed the mean *HST*/FOS spectrum and the mean optical spectrum from the 1993 monitoring campaign on the same scale in  $\lambda F_\lambda$  as best we could. They are plotted in Figure 2a. The purpose in bringing together these two high quality spectra was to place modest constraints on the strength of the predicted diffuse continuum, as presented below. The optical spectrum is the mean of a subset of the total optical data set that included only those spectra from the KAST spectrograph of the Lick Observatory spanning the duration of the *HST* portion of the 1993 campaign (K95). We forced the flux ratio  $F_\lambda(1350)/F_\lambda(5100)$  to match the mean one spanning the *HST* portion of the 1993 campaign (K95). Finally, the mean *HST* and optical spectra were dereddened with the parameters adopted from Paper I. Note that the *HST* aperture ( $4''.3 \times 1''.4$ ) was significantly smaller than the optical aperture. Thus the additive starlight contribution in the optical spectrum ( $\sim 37\%$  at  $5100 \text{ \AA}$ ; K95) will be that much larger relative to whatever weak contribution is present in the UV. We made no attempt to correct for the starlight contributions, and starlight likely accounts for the optical spectrum’s slight rise in  $\lambda F_\lambda$  toward the red for wavelengths longer than  $4200 \text{ \AA}$ , as may be perceived in Figure 2a. Notice the overall flatness of the spectrum in  $\lambda F_\lambda$ . This shape differs somewhat (it’s harder) from the SED we adopted for our photoionization calculations in Paper I and used here.

### 2.4. Model Predictions of the Diffuse Continuum Intensity

Adopting the same fit of the cloud distribution function parameters to match the mean UV line spectrum of the 1993 *HST* monitoring campaign as described in Paper I, we determined the model BLR’s integrated diffuse continuum emission in 35 wavelength bins, spanning  $400 \text{ \AA}$  to  $1.1 \text{ \mu m}$ . In brief, our model-integrated spectra included clouds distributed

spherically around the continuum source whose gas densities and distances from the central source of ionizing photons spanned  $8 \leq \log n_H \text{ (cm}^{-3}\text{)} \leq 12$  and 1 – 140 light days (see Paper I for details). We showed in Paper I that this same model was also reasonably successful in reproducing the observed UV broad emission line variability characteristics. The lower solid curve in Figure 2a shows the integrated diffuse continuum emission of the model from Paper I, appropriately scaled relative to the observed UV spectrum. To this end, the sum of the diffuse continuum plus some model for the underlying continuum (discussed below) was forced to pass through the data at 1145 Å, and the ratio of the diffuse continuum to the underlying continuum at 1215 Å then matched the ratio (0.284) predicted by the model presented in Paper I. The diffuse emission declines rapidly shortward of the Rayleigh scattering Ly $\alpha$  feature within the exponential tail of the Balmer recombination continuum; just longward of the Lyman jump, the value drops to 0.016 in units of Figure 2a. The most impressive feature is the Balmer continuum. This model predicts  $\lambda L_\lambda(3646)/L(\text{Ly}\alpha) \approx 2.7$ , as integrated over the full BLR. This is large in comparison to “classical” BLR predictions due to the contributions of high-density gas that is efficient in producing continua, but not Ly $\alpha$ . Averaged over the full UV-optical spectrum, excluding the high-contrast broad emission lines, the diffuse continuum’s contribution to the total UV/optical nuclear light is  $\sim 15\%$ .

The shape of the underlying incident continuum is not well constrained. However, in order to directly compare the approximate contribution of the predicted diffuse continuum to the data, we considered two *ad hoc* underlying continua to add to the diffuse spectrum. Our first choice was an  $F_\nu \propto \nu^{-0.7}$  ( $\lambda F_\lambda \propto \lambda^{-0.3}$ ) power law spectrum (dotted curve in Figure 2a). The UV portion of the observed spectrum is nearly flat, and this choice of power law was the flattest possible without exceeding the data at the Balmer jump, while when combined with the diffuse continuum also going through the data at 1145 Å. This also happened to be the approximate slope of the 0.2 keV – 200 keV spectrum observed by *BeppoSax* in 1997 (Nicastro et al. 2000), although it is unlikely that these power law continua could be the same. The asterisk icon in Figure 2a indicates the estimated level of the starlight-subtracted nuclear continuum at 5100 Å (Romanishin et al. 1995). Such a flat power law clearly passes well above the expected level at this wavelength. The observed flux at 5100 Å would have to lie some 27% above its plotted position in Figure 2a, in order for the nuclear continuum (underlying plus diffuse) to pass through the asterisk. Even given the uncertainties in the interspectrum normalization and level of starlight contribution, we consider this unlikely. The larger optical aperture admitted relatively *more starlight* than did the UV aperture, and our choice of interstellar extinction correction was conservative (Paper I). Thus improvements in the UV-optical intercalibration and reddening correction are more likely to push the optical spectrum a bit *lower* relative to the UV spectrum, than shown in Figure 2a. Next we chose a  $F_\nu \propto \nu^{1/3}$  ( $\lambda F_\lambda \propto \lambda^{-4/3}$ ) with an appropriate decaying

exponential to flatten and make more convex the UV spectrum in  $\lambda F_\lambda$  (dashed curve in Figure 2a). This is the rough equivalent of a classical accretion disk spectrum. When added to the diffuse continuum spectrum, the sum passes through the data at 1145 Å and very near the expected starlight subtracted flux level at 5100 Å. It also passes just underneath the bulk of the observed UV spectrum, leaving some room for overlapping broad emission line wing emission and any possible weak UV starlight contributions. The mismatch shortward of the Balmer jump may be accounted for by weak starlight and significant overlapping broad Fe II emission. It should be also noted that a spectral feature may appear in the vicinity of the Balmer jump due to the central continuum source (e.g., Hubeny et al. 2000). The mismatch just longward of the Balmer jump may be accounted for by overlapping high order Balmer line series, helium lines, Fe II emission, and some starlight. Despite the better match, however, we don't place too much confidence in this particular shape of the underlying continuum. In particular, this underlying continuum shape is almost certainly too soft shortward of  $\sim 1150$  Å, and too steep for wavelengths longer than  $\sim 6000$  Å or so, and the actual nuclear light probably lies between the dashed and dotted curves for these wavelengths (Figure 2a).

The point of the above exercise was to gain some appreciation for the relative contribution of the diffuse continuum to the total (diffuse + underlying) nuclear continuum, as illustrated in Figure 2b. At  $\lambda 1460$  the contribution is about 8%, whereas at  $\lambda 5100$  the contribution is about 20%, and at the Balmer jump it is over 40% of the total nuclear *continuum* flux. The Rayleigh scattering feature might account for part of the very broad wings of the Ly $\alpha$  broad emission line. The emission line profile decomposition of Ly $\alpha$ , the results of which were presented in K95, included the broadest wings of any of the UV emission lines, part of which may be due to Rayleigh scattering. However, additional data shortward of 1136 Å in the rest frame could prove useful in better constraining the strength of this Rayleigh scattering feature.

It is also apparent from Figures 2a,2b that the contribution from the diffuse continuum would flatten (in  $\lambda F_\lambda$ ) an intrinsically “blue” underlying UV/optical continuum. As we discussed above, it is clear that the nuclear continuum rises toward the UV (in  $\lambda F_\lambda$ ), after removing the starlight contribution from the spectrum. However, the contribution of the diffuse continuum light emerging from the BLR to the overall nuclear continuum light tends to increase toward longer wavelengths. Summing the diffuse continuum spectrum with the second choice of underlying continuum in Figure 2a changes the spectral power law slope measured between 1350 Å and 5100 Å by 0.12 ( $-0.63$  to  $-0.51$  for  $\lambda F_\lambda \propto \lambda^\beta$ ). This can be important as more sophisticated spectral models of the central continuum source are matched to the observed continua of AGN. In a later section we demonstrate how variability of the diffuse continuum can induce variability in the measured UV/optical “continuum”

slope.

In Figure 2c we show the contribution of reflected continuum light to the total (reflected plus thermal) diffuse continuous light emerging from the model BLR. Recently, Korista & Ferland (1998) discussed the UV/optical albedo of broad line clouds. Thomson scattering and Rayleigh scattering, as modified by background continuous opacity sources, predominate through the UV/optical spectrum as sources of reflection. Given the total column density of the model clouds ( $10^{23} \text{ cm}^{-2}$ ), at most  $\sim 7\%$  of the light incident upon a cloud can be scattered via electron scattering. The effective albedo will be diminished by continuous opacities, e.g., near bound-free edges where the thermal diffuse continuous emission is also strongest, and lie near their expected values where such opacities are smallest, e.g., on the longward side of the Balmer jump where the thermal diffuse continuous emission is also weak. We note that the model integrated cloud emission did not include the contributions from nearly transparent clouds of very high ionization parameter ( $U_H \gtrsim 30$ ); no UV/optical emission lines are emitted by this gas. If these clouds are present with the same distribution functions as adopted for the UV/optical emission line clouds, the diffuse continuum light in Figure 2a could be  $\sim 20\%$  higher due to electron scattering of the incident continuum by these highly-ionized clouds, except near the Balmer jump and the Rayleigh scattering feature.

Finally, while our integrated LOC model did not consider the effects of anisotropic emission from the broad line clouds (or other geometrical effects), we plot in Figure 2d the ratio of the inward to total diffuse continuum flux ratio for a slab, as weighted by the adopted model cloud distribution functions in Paper I. Davidson & Netzer (1979), Ferland et al. (1992), and O’Brien, Goad, & Gondhalekhar (1994) discussed the anisotropy of line emission from simple broad line clouds. Any reflection components will be highly anisotropic (inward/total  $\approx 1$ ), by definition, for simple slab clouds. Figure 2d shows a strong Rayleigh scattering reflection feature, but it also shows enhanced inward emission on the *long* wavelength side of the Balmer recombination continuum edge. Our model simulations show that the integrated ratio of the inward to total *thermal* diffuse continuum emission ratio is 0.52 at 3649 Å and 0.57 at 3644 Å; the UV/optical thermal diffuse continua just aren’t all that optically thick and so are emitted nearly isotropically. Thus the primary reason for the significant emission anisotropies shown in Figure 2d is the reflection of the incident continuum via Thomson and Rayleigh scattering. The more anisotropically emitting bands will be generally more sensitive to the emitter/observer geometry, and we have not considered these complications. However, to keep things in perspective, the approximate nature of the line and diffuse continuum transfer formalisms adopted in spectral simulation codes such as CLOUDY is as problematic.



## 2.5. Model Predictions of the Diffuse Continuum Reverberation

In this section we will tabulate the predicted diffuse continuum emission band –  $\lambda 1350$  continuum lags, present their light curves, and attempt to elucidate the effects of the diffuse continuum on broad emission line – continuum and continuum – continuum reverberation analyses.

### 2.5.1. Incident Continuum – Diffuse Continuum Lags

We used the observed  $\lambda 1350$  continuum light curves from the 1989 *IUE* and 1993 *IUE/HST* monitoring campaigns of NGC 5548 (Clavel et al. 1991; Korista et al. 1995) to drive our model to predict the diffuse continuum emitted by the broad line clouds as a function of time. In other words we assumed that the true driving continuum, lying mainly at ionizing energies, varies in lock-step with the  $\lambda 1350$  continuum. We weighted the response of the cloud emission by the local responsivity (see Goad, Gondhalekar, & O’Brien 1993). Once generated, we subtracted off the small diffuse continuum emission contribution from the observed light at  $\lambda 1350$  for each observation date, and then iterated using this slightly altered continuum driver. This perturbative approach should be relatively accurate, since the diffuse continuum contribution at this wavelength is small. As in Paper I we did not consider any geometrical effects, such as the anisotropy of the emission. The resulting light curves are shown in Figures 3a,3b. Other than the  $\lambda 1218$  and  $\lambda 3644$  bands that are scaled down by factors of 1.7 and 2, respectively, the light curves in Figures 3a,3b are plotted to the same scale. Note that these light curves are not just scaled versions of one another; they differ in amplitude and some of the bands’ light curves weave in and out of others. This means that the response of the diffuse continuum will ripple along in wavelength as a function of time. Of all the bands, those that lie within the hydrogen Paschen continuum (optical spectrum) respond the most coherently. Figure 3c shows the model rms variability of the diffuse continuum normalized by the mean diffuse light as a function of wavelength for both campaigns. Averaged over the full UV-optical spectrum, this normalized variability amplitude is roughly two-thirds that of the driving continuum (as represented by the continuum at  $\lambda 1350$ ). As a function of wavelength, it is in rough inverse proportion to the luminosity-weighted radius of the emission (larger regions cannot respond as coherently as smaller ones). Notice, too, that the strongest diffuse continuum variations are expected (1) underneath the C IV  $\lambda 1549$  emission line, (2) just longward of the Balmer jump, and (3) shortward of  $\sim 1100 \text{ \AA}$ . However, Figure 2b shows that the diffuse continuum is also weak within each of these spectral regions.

Next, we computed the local responsivity-weighted lags for the diffuse continuum bands

relative to the corrected  $\lambda 1350$  continuum; these are plotted as a function of wavelength in Figure 4, and tabulated in Table 1 for those bands plotted in Figure 1. These lags are determined from the cross-correlation functions computed over the entire duration of each of these two UV campaigns (White & Peterson 1994). Note that the lags differ for the two campaigns — this is due to the differences in the continuum variability characteristics of each of the two campaigns. Figure 4 and Table 1 indicate that one should expect lags characteristic of the inner broad emission line region, overlapping with the emission line lags of Ly $\alpha$ , C IV  $\lambda 1549$ , Si IV  $\lambda 1400$ , and for spectral bands shortward of  $\sim 1070$  Å — more characteristic of N V  $\lambda 1240$  and He II  $\lambda 1640$ . The Rayleigh scattering feature, effectively due to the extreme damping wings of the Ly $\alpha$  emission transition, will have lags relative to the incident continuum that mimic that of the broad emission line of Ly $\alpha$  itself. Like the Ly $\alpha$  emission line, the Rayleigh scattering feature is expected to be emitted highly anisotropically, though our model does not take this geometrical complexity into account.

Maoz et al. (1993) found an overall lag of  $\sim 10$  days between diffuse emission components in the “small blue bump” (after subtracting off an estimate to the underlying continuum) and the  $\lambda 1350$  continuum during the 1989 campaign. This is similar to our model’s predictions given in Table 1 and Figure 4, with an important caveat being that their derived diffuse emission light curves included the pseudo-continuum emission of Fe II in addition to the Balmer continuum. The last column of Table 1 in Maoz et al., labeled “Opt1,” lists their measurements of the diffuse light flux between 3245 Å and 3635 Å over the duration of the 1989 campaign, temporally sparse as they were. They considered this band to contain primarily Balmer continuum. The mean of their measurements is approximately  $2.8 \times 10^{-12}$  ergs s $^{-1}$  cm $^{-2}$  (rest-frame). If we divide this wide-band flux by the width of the band (390 Å) and then multiply by the central wavelength of the band (3440 Å), we find an approximate mean value of the diffuse flux  $\lambda F_{\lambda}(3440) \approx 2.9 \times 10^{-11}$  ergs s $^{-1}$  cm $^{-2}$  (corrected for reddening, rest frame). This is very nearly the model’s time-averaged value for  $\lambda F_{\lambda}(3644) = 2.7 \times 10^{-11}$  ergs s $^{-1}$  cm $^{-2}$  for the 1989 campaign; see bottom panel of Figure 3a. In addition the variability amplitude for this model diffuse continuum band is 1.7, in good agreement with the value measured by Maoz et al. for their “Opt1” component (1.6). The model developed in Paper I was not constrained by any information pertaining to the Balmer continuum. Nevertheless, the model does remarkably well in predicting the Balmer continuum’s overall strength and general variability characteristics.

Summarizing: wavelength dependencies in variability amplitude and lag for the diffuse continua are to be expected. The exponential nature of the bound-free emissivity sensitivity to temperature sets the run of the luminosity-weighted radius vs. wavelength (at wavelengths where the thermal continua dominate). This means that the lag,  $\tau(\lambda)$ , of the diffuse continuum relative to the ionizing continuum is a generally increasing function of wavelength

across the UV-optical spectrum. *This general result is not all that sensitive to the choice of model of the broad line region, but is a simple result of the gas thermodynamics.*

### 2.5.2. Inter-Band Continuum Lags

What effect does a variable diffuse continuum have upon the measurements of the so-called “continuum” windows? To investigate this, one can simply assume that the underlying nuclear continuum varies coherently with wavelength, and then dilute the delay signal of the diffuse continuum light (Figure 4) by multiplying this by the mean fraction of the diffuse light to the underlying nuclear continuum light at each wavelength. The results for both assumptions of the underlying continuum are shown in Figure 5a,5b. Here it is shown that the  $\lambda 1460$  continuum band lies near the minimum in the curves shown, with a lag of 0.3–0.5 days relative to an unpolluted underlying continuum. This lag is also typical for the spectral region between 1350 Å and 1600 Å. However, at 5100 Å the measured continuum may lag behind the ionizing continuum by 1–2 days. Thus the characteristic lag of the broad H $\beta$  emission line, whose light curve is generally cross-correlated with the continuum band at 5100 Å, may actually be a bit longer relative to the ionizing continuum than has been reported. Comparison of these UV and optical continuum band lags leads to an UV-optical inter-band ( $\lambda 1350 - \lambda 5100$ ) continuum lag of approximately 0.6–1.7 days, again assuming that the underlying UV-optical continuum varies coherently. Larger (smaller) UV-optical inter-band lags would be expected if the underlying UV-optical continuum exhibited a lag relative to the ionizing continuum proportional (inversely proportional) to wavelength (see Wanders et al. 1997; Collier et al. 1999). K95 found a possible lag between  $\lambda 1350$  and  $\lambda 5100$  of 0.7–1.2 days (the latter lagging behind the former) in NGC 5548, with significant uncertainty due to the 1 day time-sampling of the campaign. Monte Carlo simulations indicated a 1.2 day upper limit (90% confidence level) to any inter-band continuum lag present in the data. The results presented here suggest that such a lag may be real and due primarily to diffuse continuum emission from the BLR. They would also suggest that this diffuse continuum is at least partially responsible for the systematic changes in the amplitude and sharpness within the UV continuum band light curves presented in K95. It should also be noted that the typically-chosen continuum windows are likely contaminated with emission from weak lines and overlapping wings of strong lines at levels that could rival the diffuse continuum in some of the weaker diffuse continuum bands.

Hard evidence of a wavelength-dependent UV/optical interband continuum lag was found in NGC 7469 by Wanders et al. (1997), and confirmed by Collier et al. (1999) and Kriss et al. (2000). The relationship was found to be consistent with that expected by the

reprocessing of X-rays illuminating an accretion disk:  $\tau(\lambda) \propto \lambda^{4/3}$  (see also Nandra et al. 2000 for a description of X-ray/UV variability). However, note the similarity of this relationship, also plotted in Figure 5, to the model  $\tau(\lambda)$  relation that considers the contribution of a variable diffuse continuum from the BLR to a coherently varying underlying continuum. These results bring into question the interpretation of the origin of the wavelength-dependent interband continuum lags. Indeed, Figure 14 in Kriss et al. (2000) shows that their longest wavelength UV continuum bands’ lags are systematically too high compared to the illuminated disk model, in just the way expected if there were significant contamination from diffuse Balmer continuum from the BLR. The uncertainties in the measured continuum band lags will need to be reduced substantially to determine whether or not the accretion disk reprocessing scenario is the correct one, and/or better constrain the diffuse continuum emission in AGN. For the time being it would be prudent not to ignore the contribution of the diffuse continuum from the same gas that emits the lines to the variable spectra of AGN.

### 2.5.3. *Bluer When Brighter*

First noticed in NGC 5548 by Wamsteker et al. (1990), and again by Maoz et al. (1993) and Korista et al. (1995), the UV/optical continuum, as measured between  $\lambda 1350 - \lambda 5100$ , becomes bluer as it becomes brighter. This effect has also been observed in the behavior of other Seyfert nuclei variability, though apparently not in Fairall 9 (see Santos-Lleó et al. 1997). The nature of this effect has lain in some doubt due to known contamination from non-variable sources of light, such as starlight that is important primarily at the longer wavelengths. However, Romano & Peterson (1998) find this effect to remain even after subtracting a range of estimates for starlight contribution at  $5100 \text{ \AA}$ , at least in the case of NGC 5548. For the starlight contribution determined observationally by Romanishin et al. (1995), and adopted here, Romano & Peterson find the relation  $\alpha_{1350/5100} = -6.09 \times 10^{-3} F_{\lambda 1350} + 0.800$ , with  $F_{\nu} \propto \nu^{-\alpha}$  defining the logarithmic slope and  $F_{\lambda 1350}$  in units of  $10^{-15} \text{ ergs cm}^{-2} \text{ s}^{-1} \text{ \AA}^{-1}$ . Their relationship did not take reddening into account, but this affects only the intercept of their relation. If intrinsic to the nuclear light, the nature of this relationship is telling us something important about the central continuum source. A continuum that becomes bluer when brighter may be indicative of X-ray heating of an accretion disk, for example.

Figure 6a shows the ratio of the flux ( $\lambda F_{\lambda}$ ) at  $\lambda 1350$  to that at  $\lambda 5100$ , after adding the model diffuse continuum light for each date of the 1989 *IUE* campaign to the underlying continuum at each of the two wavelength bands. We used the second assumption for the underlying continuum in Figure 2a as a model for the underlying UV/optical continuum.

The underlying UV/optical continuum’s value at 1350 Å was very nearly the measured value (corrected by a small amount of diffuse light), and as pointed out above, its value at 5100 Å added to the diffuse light there is nearly equal to the starlight subtracted flux. (Whether or not we corrected the  $\lambda 1350$  light curve for a small amount of diffuse continuum emission had very little impact on the results presented here.) The model underlying continuum’s shape was held fixed, and had a logarithmic slope of  $\alpha_{1350/5100} = 0.363$  ( $F_\nu \propto \nu^{-\alpha}$ ). Figure 6a shows that the predicted flux ratio fluctuates by  $\pm 5\%$  about a mean of 1.98, and is correlated with the underlying continuum at  $\lambda 1350$  at the 87% level with the ratio leading the underlying continuum by a couple of days (see also the top panel of Figure 3a). In other words, the effective nuclear light becomes bluer when it becomes brighter due to the reverberation of the diffuse continuum within the BLR. The same effect was seen in similar simulations of the 1993 *HST* campaign, with slightly smaller fluctuations about a mean ratio of 1.91, again with the continuum flux ratio leading slightly the underlying continuum. Figure 6b shows the effective logarithmic slope,  $\alpha_{1350/5100}$ , as a function of the flux of the underlying continuum at  $\lambda 1350$  for both monitoring campaigns. The effective slope was determined from the flux ratio above, and so considers the sum of the underlying plus diffuse continuum components. We adopted the same format as in Figure 3 of Romano & Peterson to ease comparison. This slope is highly correlated with the underlying  $\lambda 1350$  continuum in both campaigns, though with differing relationships — likely due to the differences in the continuum variability characteristics of each of the two campaigns. Note, too, that the effective logarithmic slope may deviate from that of the underlying continuum (0.363) by up to 0.2 (with  $\alpha_{eff}(\max) \sim 0.56$ ), with the total UV/optical continuum light being significantly softer than the underlying nuclear continuum. Greatest deviations between the underlying and effective UV/optical slopes are expected when the underlying continuum is *low* (assuming that the ionizing and underlying continua are well-correlated). Figure 3c shows that the diffuse continuum at 1350 Å is somewhat more variable and Figure 4 shows it to have a smaller lag than the diffuse continuum at 5100 Å. The diffuse continuum is less variable than the underlying continuum at all wavelengths. Taken together these account for the results presented in Figures 6a,6b. However, comparing the slopes of the lines fitted to the points in Figure 6b to the slope of the relation found by Romano & Peterson (above), one sees that the reverberation of the diffuse continuum emitted by the BLR can account for only  $\sim 1/3$  of the observed effect, meaning that the underlying continuum likely does become bluer as it becomes brighter. What we have demonstrated here is that not all of this effect should be automatically attributed to the underlying continuum.

### 3. DISCUSSION & SUMMARY

#### 3.1. The Rayleigh and Electron Scattering Features

The shortest wavelength continuum band reported by K95,  $\lambda 1145$ , lies within the blue wing of the predicted Ly $\alpha$  Rayleigh scattering feature in Figure 2a. In the spectrum from any single cloud the width of this feature is proportional to the neutral column density (Korista & Ferland 1998), and unlike all other features in the diffuse continuum spectrum, it is observed only in reflection. While the light curve data in this band were noisy, K95 reported that this band had the largest amplitude and sharpest variations, though neither characteristic was much different from those in the  $\lambda 1350$  band. Nevertheless, based upon the observed characteristics of the light curves one might expect less contamination of diffuse continuum emission from the BLR within the  $\lambda 1145$  band than elsewhere, in possible contradiction to the model results. Extending the observed spectral coverage to shorter wavelengths should help constrain the model predictions of this scattering feature. It is also clear that this feature contributes to the measured Ly $\alpha$  broad emission line flux and has similar reverberation properties.

The effects of electron scattering on the diffuse continuum spectrum are fairly minimal in these simulations given our choice of constant column density clouds with  $\log N_H = 23$  (see Figure 2c). As mentioned above, however, most of the anisotropy in the diffuse emission from the clouds (Figure 2d) is expected to arise from the electron scattering component (well outside the Rayleigh scattering feature). For wavelengths well longward of the Ly $\alpha$  Rayleigh scattering feature ( $\lambda \gtrsim 1800 \text{ \AA}$ ) the reflected-light component of the diffuse continuum, mainly Thomson scattering of the incident continuum, has a luminosity-weighted radius that is roughly 30% that of the Ly $\alpha$  emission line and the peak of the Rayleigh scattering feature (all of which are predicted to be heavily inwardly beamed). This is expected in models that geometrically weight the contributions of light from clouds nearer to the continuum source — the stronger electron-scattering mirrors are those clouds with larger ionized hydrogen column densities. The expected lag of this reflected-light component is very nearly independent of wavelength across the UV/optical spectrum, in contrast to that of the thermal diffuse light for which the lag generally increases with wavelength, and whose emission is expected to be much less anisotropic. Thus larger contributions from electron scattering of the incident continuum off the broad line clouds (1) will result in a greyer response; (2) the anisotropic nature of the electron-scattered light may increase the amplitude of the response by reducing the range in time-delays over which we see the diffuse light; (3) the anisotropic nature of the electron-scattered light will offset the electron-scattered light’s tendencies to have smaller luminosity-weighted radii than the thermal diffuse continuum.

### 3.2. The Lyman and Balmer Continua

The model predicts a Lyman jump in emission with an intensity similar to that of the peak of the Ly $\alpha$  Rayleigh scattering feature in Figure 2a, amounting to a  $\sim 25\%$  jump in the total nuclear light near 912 Å, assuming the underlying continuum is featureless in the vicinity of the jump. After considering spectral broadening due to bulk gas motions, this jump might only be  $\lesssim 20\%$  — but still easily observable. Our model  $\lambda L_\lambda(912)/L(\text{Ly}\alpha)$  is roughly 2.4, large in comparison to “classical” BLR predictions due to the contributions of high-density gas ( $n_H > 10^{10} \text{ cm}^{-3}$ ) that is efficient in producing continua, but not Ly $\alpha$ . It is important to note that the prediction of a Lyman feature in emission is generic to virtually all spectral simulations of the broad-line emitting gas. However, while the Balmer continuum is observed within the little blue bump, the Lyman continuum is *never* observed. In fact the quasar spectra in this region are remarkably featureless (Koratkar & Blaes 1999), with only hints of a small *depression* near 912 Å in some objects (e.g., Kriss et al. 1995). This has been a long-standing puzzle for models of both broad line clouds and accretion disks, though the more recent considerations of Comptonization (Kriss et al.) and non-LTE effects (Hubeny et al. 2000) generally produce weaker absorption features in the vicinity of the Lyman limit than the earlier models of accretion disk spectra. As averaged over our BLR model, some 90% of the diffuse continuum at the Lyman jump is beamed inward, and perhaps this plays some role in hiding it from view. It is also conceivable that a conspiracy of sorts exists whereby the accretion disk feature in absorption near 912 Å counteracts the feature expected in emission from the broad line gas, as suggested by Carswell & Ferland (1988). But these are rather unsatisfying scenarios, and we must admit we do not have a good understanding of the Lyman continuum spectral feature.

Since the Balmer continuum is observed in emission, an understanding of its origin would constrain models of broad emission line gas as well as those of accretion disks — the Balmer continuum could appear in emission in a chromosphere of an accretion disk. If the Balmer continuum is emitted primarily in the BLR, a significant lag ( $\sim 1$  week for NGC 5548) is expected between flux variations in the emission near the jump and those of the underlying continuum. If, on the other hand, the Balmer continuum is emitted in the chromosphere of an illuminated accretion disk, the lags would be expected to be much smaller. In fact in this case, the wavelength-dependent interband continuum lag would deviate from the simple  $\lambda^{4/3}$  relationship, and behave in a way similar to that presented in Figure 5a except that the lags should be much smaller across the Balmer continuum. The results of the analysis of Maoz et al. (1993) would appear to favor an origin in the BLR, but this must be confirmed with follow-up observations of NGC 5548 and other AGN. Weak Balmer and Paschen continua from broad line gas is a signature of either the predominance of low density gas ( $n_H \ll 10^{12} \text{ cm}^{-3}$ ), or the presence of a mechanism that broadens the

local line profiles significantly above their thermal values. Local line broadening reduces the line optical depths, effectively increasing the cooling efficiency of the lines. Bottorff et al. (2000) explored the effect of local line broadening to quasar spectra. Simulations from that work (Bottorff 2000) and some of our own show that by increasing the local line width from thermal to  $1000 \text{ km s}^{-1}$ , the model luminosity of the Balmer jump ( $\lambda L_{\lambda}(3646)$ ) falls by a factor of 2.5, and its ratio with respect to the luminosity of  $\text{Ly}\alpha$  falls by a factor of 4.8. In addition, the strength of the Balmer jump relative to  $\text{Ly}\alpha$  and the strengths of the diffuse recombination continua in general are very sensitive to the presence and importance of high density gas ( $n_H > 10^{10} \text{ cm}^{-3}$ ), especially if the local line widths are thermal. The presence of super-solar metallicity gas would also diminish the thermal diffuse continua, due to the accompanying decreases in electron temperatures, though these metallicities are not expected to occur in Seyfert 1 nuclei. Again, we emphasize that these trends are general and not dependent upon our particular model of the BLR of NGC 5548. It is clear that the under-explored Balmer continuum should be mined for its important physical constraints.

### 3.3. Interband Continuum Variations in Other AGN

Short, but intense, multiwavelength monitoring campaigns have been mounted to detect correlated variability amongst the various energy bands (X-ray, UV, optical) emitted by Seyfert 1 nuclei. Edelson et al. (1996) reported good correlations between X-ray, UV, and optical continuum variations during the 9-day monitoring campaign of NGC 4151, but could not measure any lags within or between any of these bands, and set a limit of  $\lesssim 1$  day lag between  $\lambda 1275$  and  $\lambda 5125$ . In the 3-day campaign of NGC 3516 Edelson et al. (2000) reported correlated hard and soft X-ray variations and correlated optical variations, but the X-ray and optical bands showed very different variability behavior. They set a limit of  $\lesssim 0.15$  day lag between the  $\lambda 3590$  and  $\lambda 5510$  bands, and suggested that their findings represent serious problems for “reprocessing” models in which the X-ray source heats the accretion disk. It is unlikely that either of these experiments were long enough for the continuum variations to sufficiently sample the BLRs in order to detect variations from the diffuse continuum. This is in contrast to the high temporal resolution campaign of NGC 7469 that spanned 50 days. As discussed above, significant lags were found across its UV and optical continuum bands, and were found to be consistent with a simple model of an X-ray illuminated accretion disk. However, the results presented here suggest that this conclusion may be premature, as the variable diffuse continuum from the BLR may broadly mimic the signature of an X-ray heated accretion disk.



### 3.4. Summary

Unless some mechanism is present that acts to suppress the emission of diffuse thermal continua, that which is emitted in the UV/optical by broad line clouds will be significant. Its presence in combination with the light reflected from the broad line clouds has the following impacts on models for the broad emission line region and the UV-optical continuum emitter: (1) the lag between the emission line variations and those of the local “continuum” may underestimate the characteristic sizes of the line emitting regions, (2) the shape of the underlying nuclear continuum may be misinferred and thus misinterpreted, (3) interband continuum lags may be misinterpreted, (4) the reverberation of the diffuse continuum emitted by the BLR may account for perhaps one-third of the observed effect that the  $\lambda 1350 - \lambda 5100$  continuum becomes bluer as it becomes brighter (even after accounting for non-variable optical starlight), and (5) as in other models of the broad emission line gas, a significant yet unobserved Lyman jump is predicted. The underexplored diffuse continuum, most easily observable near the Balmer jump, holds clues to our understanding of both the line and central continuum emitting regions in AGN. Long-term, high temporal resolution, spectroscopic monitoring with full UV-optical spectral coverage is required to understand the nature of UV-optical continuum and its variability in AGN. This can be accomplished with a dedicated multiwavelength orbital platform.

We are grateful to Gary Ferland for maintaining his freely distributed code, CLOUDY, to Brad Peterson for supplying the mean optical spectrum of NGC 5548, and to Mark Bottorff for supplying some spectral simulation results. We also acknowledge helpful conversations with Stefan Collier, and the constructive comments of an anonymous referee.

## REFERENCES

- Baldwin, J.A., Korista, K.T., Ferland, G.J., & Verner, D.A. 1995, *ApJ*, 455, L119
- Bottoff, M. 2000, private communication
- Bottoff, M., Ferland, G., Baldwin, J., & Korista, K. 2000, *ApJ*, 542, 644
- Carswell, R.F., & Ferland, G.J. 1988, *MNRAS*, 235, 1121
- Clavel, J., et al. 1991, *ApJ*, 366, 64
- Collier, S. Horne, K., Wanders, I., & Peterson, B.M. 1999, *MNRAS*, 302, 24
- Davidson, K. 1976, *ApJ*, 207, 710
- Davidson, K., & Netzer, H. 1979, *Rep. Prog. Phys.*, 51, 715
- Edelson, R., et al. 1996, *ApJ*, 470, 364
- Edelson, R., et al. 2000, *ApJ*, 534, 180
- Ferland, G.J., Peterson, B.M., Horne, K.D., Welsh, W.F., & Nahar, S.N. 1992, *ApJ*, 387, 95
- Ferland, G.J., 1997, *HAZY*, A Brief Introduction to *CLOUDY* (Univ. Kentucky Phys. Dept. Int. Rep.)
- Ferland, G.J., Korista, K.T., Verner, D.A., Ferguson, J.W., Kingdon, J.B., & Verner, E.M. 1998, *PASP*, 110, 761
- Goad, M.R., O'Brien, P.T., & Gondhalekar, P.M. 1993, *MNRAS*, 263, 149
- Hubeny, I., Algol, E., Blaes, O., & Krolik, J.H. 2000, *ApJ*, 533, 710
- Kaspi, S., & Netzer H. 1999, *ApJ*, 524, 71
- Koratkar, A., & Blaes, O. 1999, *PASP*, 111, 1
- Korista, K.T., et al. 1995, *ApJS*, 97, 285 (K95)
- Korista, K., Baldwin, J., Ferland, G., Verner, D. 1997, *ApJS*, 108, 401
- Korista, K., & Ferland, G. 1998, *ApJ*, 495, 672
- Korista, K.T., & Goad, M.R. 2000, *ApJ*, 536, 284
- Kriss, G.A., et al. 1995, *ApJ*, 444, 632
- Kriss, G.A., Peterson, B.M., Crenshaw, D.M., & Zheng, W. 2000, *ApJ*, 535, 58
- Maoz, D., et al. 1993, *ApJ*, 404, 576
- Nandra, K., Le, T., George, I.M., Edelson, R.A., Mushotzky, R.F., Peterson, B.M., & Turner, T.J. 2000, *ApJ*, in press
- O'Brien, P.T., Goad, M.R., & Gondhalekar, P.M. 1994, *MNRAS*, 268, 845

- Romanishin, W. et al. 1995, ApJ, 455, 516
- Rees, M.J., Netzer, H., & Ferland, G.J. 1989, ApJ, 347, 640
- Romano, P., & Peterson, B.M. 1998, ApJ, in preparation, (astro-ph/9806190)
- Santos-Lleó, M., et al. 1997, ApJS, 112, 271
- Wamsteker, W., et al. 1990, ApJ, 354, 446
- Walter, R., Orr, A., Courvoisier, T.J.-L., Fink, H.H., Makino, F., Otani, C., Wamsteker, W.  
1994, A&A, 285, 119
- Wanders, I., et al. 1997, ApJS, 113, 69
- White, R.J. & Peterson, B.M., 1994, PASP, 106, 879

Fig. 1a.— Contours of theoretical  $\log[\lambda F_\lambda(\text{diffuse})/\lambda F_{\lambda 1215}(\text{incident})]$  for 6 diffuse continuum bands are shown in the plane of hydrogen gas density and flux of hydrogen ionizing photons. The total hydrogen column density is  $10^{23} \text{ cm}^{-2}$ , and each point in the grid assumes full source coverage. The smallest, generally outermost, solid decade contours correspond to a ratio of 0.1, solid lines are decades, and dotted lines represent 0.1 decade steps between. The contours generally decrease monotonically from the peak (solid triangle, with ratio values  $\sim 1$  at very high gas densities and photon fluxes) to the ratio = 0.1 contour. The solid star is a reference point marking the old “standard BLR” parameters.

Fig. 1b.— Same as Figure 1a for 6 more diffusing continuum bands.

Fig. 2a.— The mean, dereddened UV-optical spectrum of NGC 5548 from the 1993 *HST* campaign (top, solid), the appropriately scaled model diffuse continuum (bottom, solid), and the sum of the latter and two guesses to the underlying nuclear continuum (middle):  $\lambda F_\lambda \propto \lambda^{-0.3}$  (dotted),  $\lambda F_\lambda \propto \lambda^{-4/3} e^{-\lambda_{cut}/\lambda}$  (dashed). The most prominent features in the diffuse continuum are the Balmer continuum and the Ly $\alpha$  Rayleigh scattering feature. The Paschen continuum dominates the optical regime. The asterisk represents the approximate starlight-subtracted continuum flux level at 5100 Å.

Fig. 2b.— The fractional contribution of the diffuse continuum to the sum diffuse plus underlying continua for both models of the underlying continuum. Dashed and dotted symbols refer to the corresponding underlying continua assumed in Figure 2a.

Fig. 2c.— The fractional contribution of the reflected incident continuum to the total diffuse light emerging from the model BLR.

Fig. 2d.— The integrated LOC model ratio of the inward to total diffuse continuum flux emitted by the slab-cloud geometry assumed in the CLOUDY computations as a function of wavelength. Values of 0.5 indicate isotropic emission, whereas values of 1 indicate fully inwardly beamed emission.

Fig. 3a.— Top panel: the measured, rest frame, reddening corrected, continuum light curve at 1350 Å from the 1989 *IUE* campaign of NGC 5548, corrected also for the diffuse continuum emission at 1350 Å. Bottom two panels: model diffuse continuum light curves using the continuum in the top panel as the driver of the BLR response.

Fig. 3b.— Same as Figure 3a but for the 1993 *HST* campaign.

Fig. 3c.— The model rms variation normalized by the mean light for the diffuse continuum as a function of wavelength for the 1989 (bold) and 1993 (thin) campaigns. The rms variation is roughly inversely proportional to the luminosity-weighted radius of the diffuse continuum emission.

Fig. 4.— The wavelength-dependent lag of the diffuse continuum relative to the corrected  $\lambda 1350$  continuum driver. The bold solid and dashed lines are the model peak and centroid CCF lags derived using the corrected  $\lambda 1350$  continuum of the 1989 *IUE* campaign as the driver. The thin solid and dashed lines are the model peak and centroid CCF lags derived using the corrected  $\lambda 1350$  continuum of the 1993 *HST/IUE* campaign as the driver.

Fig. 5a.— Same as Figure 4, but with the lags scaled by the ratio of the diffuse continuum to the underlying continuum. Here it is assumed that the underlying continuum varies *coherently* in wavelength, and it has the form  $\lambda F_\lambda \propto \lambda^{-0.3}$  (see Figure 2a). Differences in lag should be representative of the lag measured between the light curves of any two so-called continuum windows. The extra-bold dash-dotted curve is the function  $\tau(\lambda) = 3(\lambda/10^4 \text{Å})^{4/3}$  from Kriss et al. (2000).

Fig. 5b.— Same as Figure 5a, but assuming an underlying continuum of the shape  $\lambda F_\lambda \propto \lambda^{-4/3} e^{-\lambda_{cut}/\lambda}$  (see Figure 2a). The extra-bold dash-dotted curve is the function  $\tau(\lambda) = 4.5(\lambda/10^4 \text{Å})^{4/3}$ .

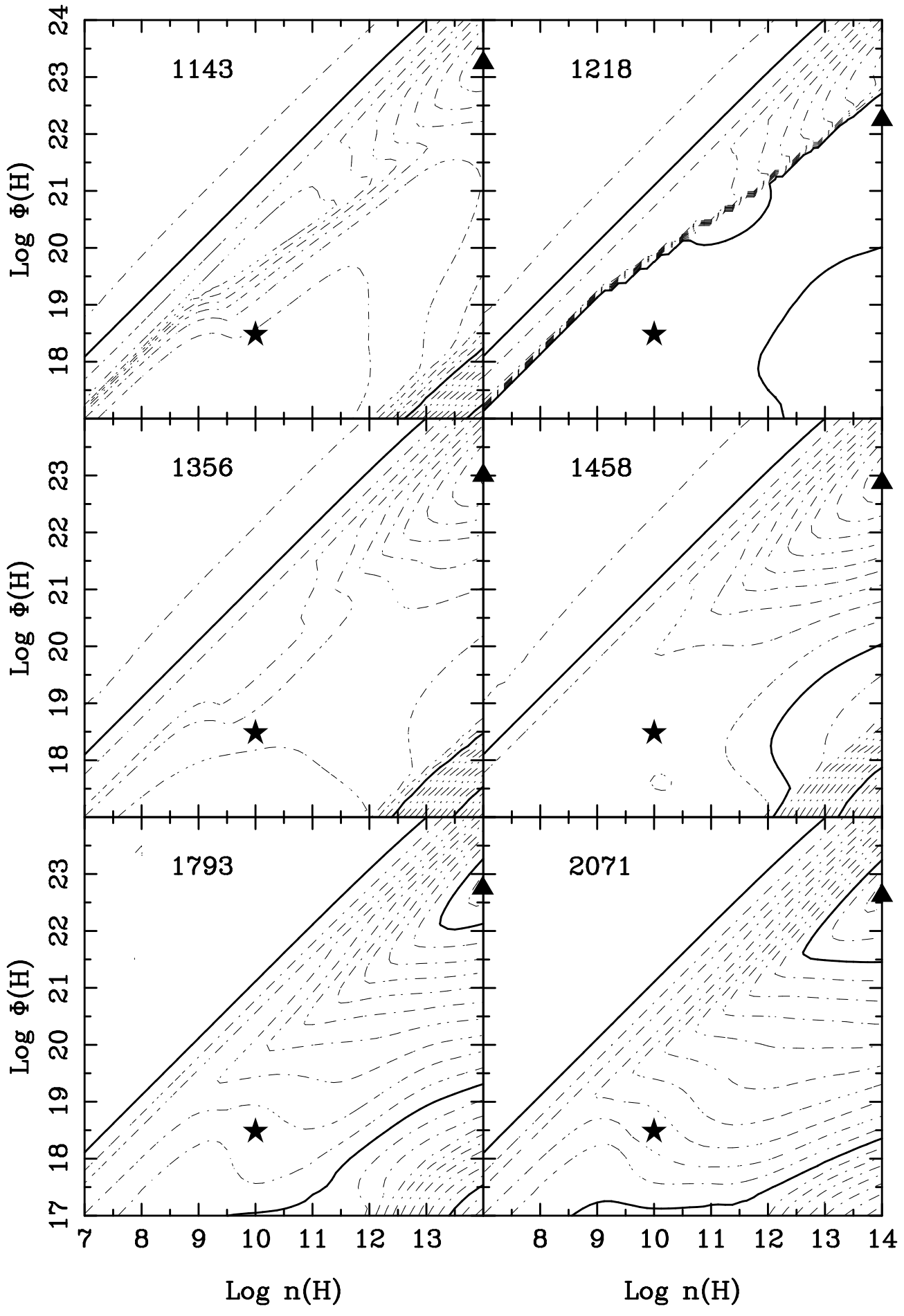
Fig. 6a.— The ratio of the model diffuse plus underlying continua at  $1350 \text{ Å}$  to that at  $5100 \text{ Å}$  as a function of time, for the 1989 *IUE* campaign. This ratio is highly positively correlated with the flux at  $1350 \text{ Å}$ , and so the  $\lambda 1350 - \lambda 5100$  continuum becomes bluer as the underlying continuum becomes brighter.

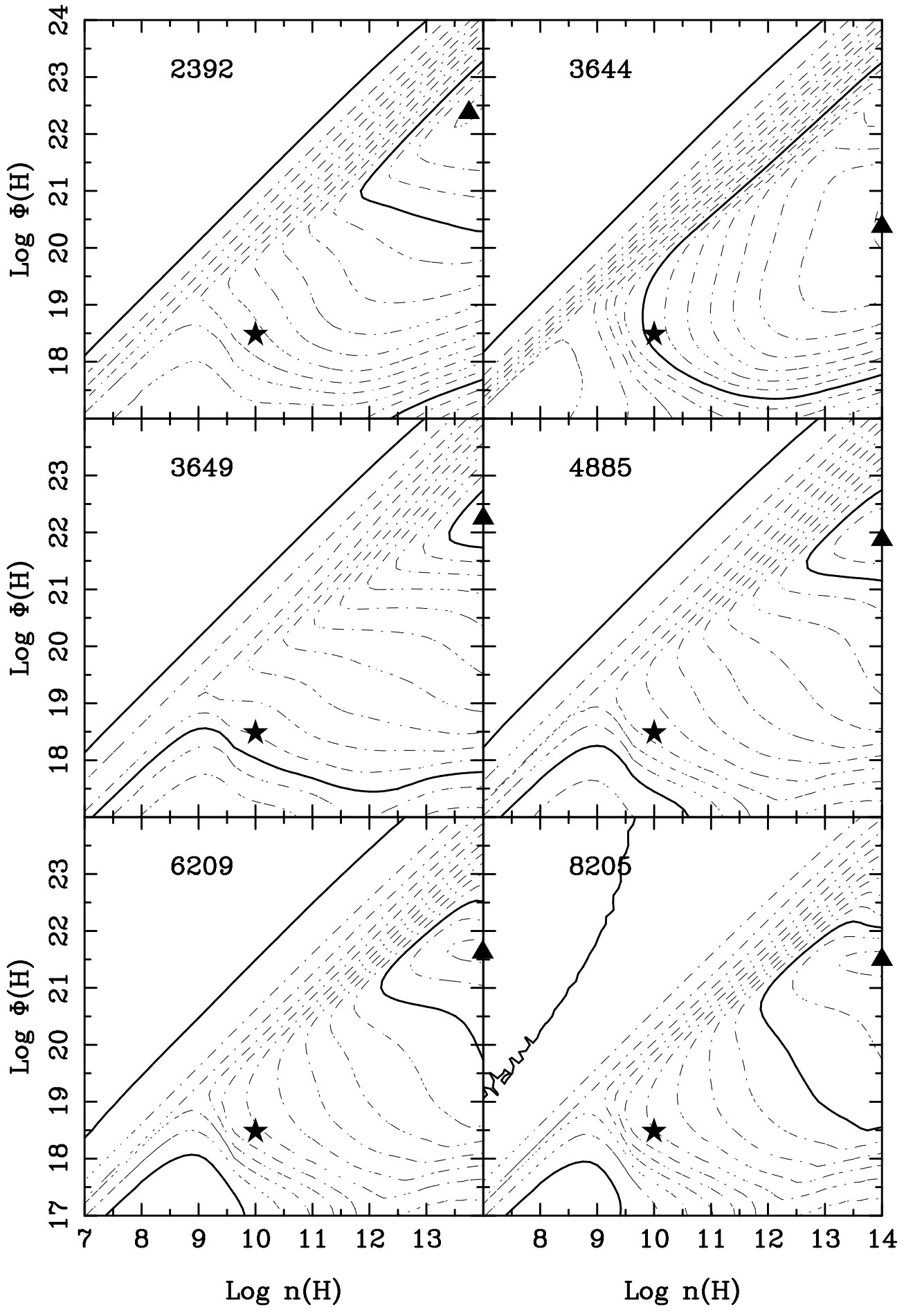
Fig. 6b.— The logarithmic slope,  $\alpha_{1350/5100}$ , as a function of the flux at  $\lambda 1350$  for both monitoring campaigns (squares: 1989 *IUE*; triangles: 1993 *HST*). Simple linear fits are also shown for each. The logarithmic slope of the model underlying continuum was fixed at  $\alpha_{1350/5100} = 0.363$  ( $F_\nu \propto \nu^{-\alpha}$ ).

Table 1. Model Diffuse Continuum Band Lags.

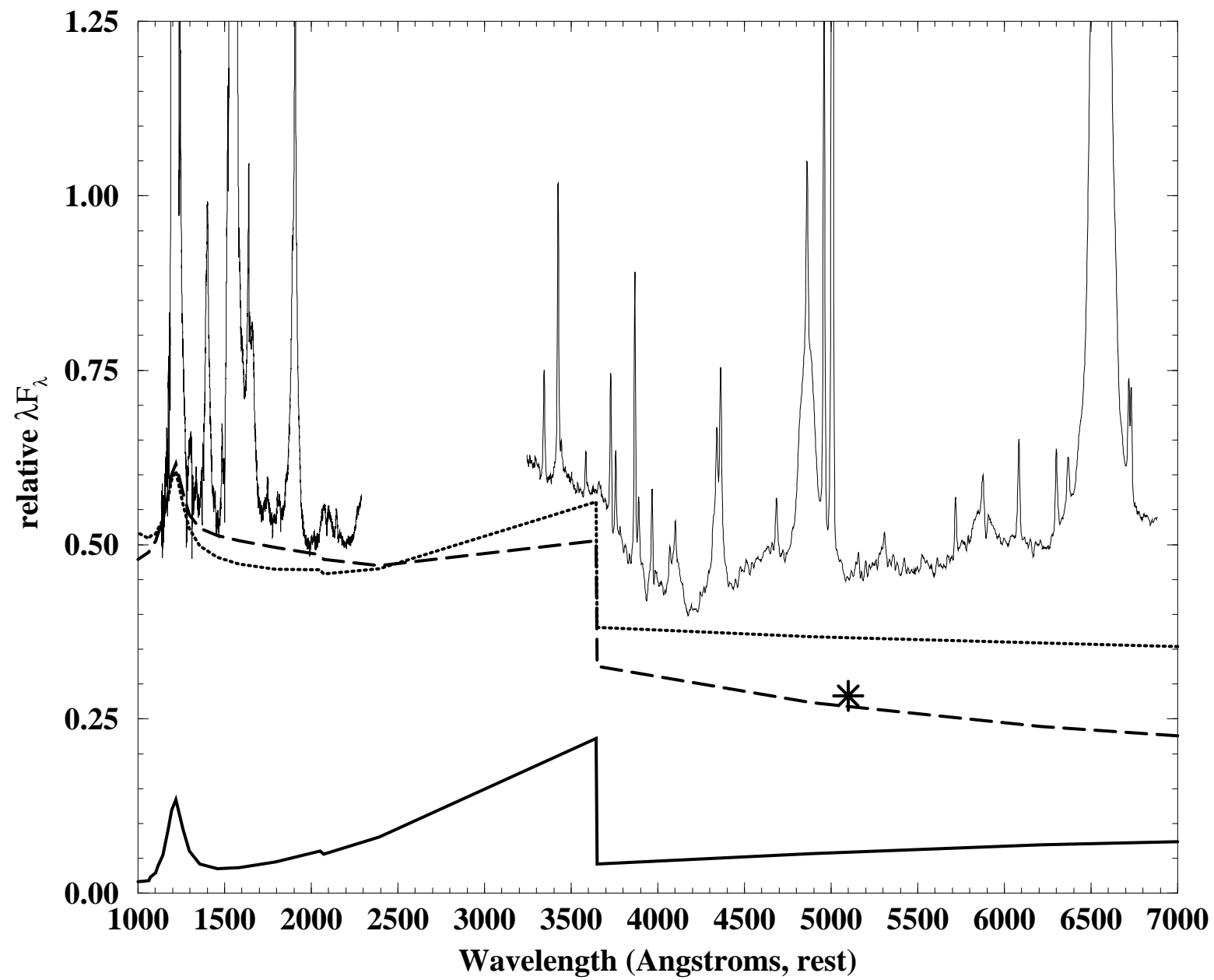
| Wavelength     | $\tau_\eta(IUE89)$ | $\tau_\eta(HST93)$ |
|----------------|--------------------|--------------------|
| $\lambda 1143$ | 5.3–6.1            | 3.5–6.5            |
| $\lambda 1218$ | 9.7–10.6           | 6.5–9.4            |
| $\lambda 1356$ | 4.9–5.2            | 3.4–6.0            |
| $\lambda 1458$ | 4.8–4.9            | 3.4–5.9            |
| $\lambda 1793$ | 5.2–5.6            | 3.6–6.5            |
| $\lambda 2071$ | 5.7–6.3            | 4.5–7.2            |
| $\lambda 2392$ | 6.2–7.6            | 5.4–7.9            |
| $\lambda 3644$ | 10.0–11.1          | 7.5–10.2           |
| $\lambda 3649$ | 5.4–6.0            | 4.4–6.8            |
| $\lambda 4885$ | 6.0–7.0            | 4.6–7.5            |
| $\lambda 6209$ | 6.3–7.9            | 5.4–8.0            |
| $\lambda 8205$ | 6.7–8.6            | 5.5–8.5            |

Note. — The local responsivity-weighted CCF lags,  $\tau_\eta$ , are given in units of days. Each pair of lags relative to the driving continuum ( $\lambda 1350$ ) is given as “CCF peak – CCF centroid,” the latter measured at 50% of the CCF peak. All lags have been determined from the full durations of the campaigns.









\*

